crystals

MDPI

Article

Research on the Fabrication of X-Cut Near Stoichiometric Lithium Niobate Wafers

Zixuan Dong [1,2,3,4], Qingyan Xu [1,2,3], Shuaijie Liang [3,5], Jiashun Si [3,5], Mengfan Wang [1,2,*], Xuefeng Zhang [1,2,3] and Jilin He [1]

[1] School of Materials Science and Engineering, Zhengzhou University, Zhengzhou 450001, China; dzxgogogo7128@163.com (Z.D.); xuqingyan97@163.com (Q.X.); zxf905@126.com (X.Z.); hejilin@zzu.edu.cn (J.H.)
[2] Zhongyuan Critical Metals Laboratory, Zhengzhou 450001, China
[3] Ningxia Ju Jing Yuan Crystal Technology Company Limited, Shahu Road 304, Shizuishan 753000, China; liangxuzhi188@163.com (S.L.); sijias0121@163.com (J.S.)
[4] School of Physics and Optoelectronic Engineering, Taiyuan University of Technology, Taiyuan 030024, China
[5] College of Electric and Information Engineering, North Minzu University, Wenchang Road 204, Yinchuan 750021, China
* Correspondence: mengfanwang1995@163.com

Abstract: This article discusses the preparation of twin free X-cut lithium niobate wafers using the diffusion method. The liquid electrode method was used to eliminate parasitic microdomains at dislocations. According to research, the Li-rich lithium niobate polycrystalline material contains ($Li_{0.941}Nb_{0.059}$) $Nb_{0.9528}O_3$ and Li_3NbO_4 phases, and the diffused near-stoichiometric lithium niobate wafer exhibits a monodomain state. The piezoelectric coefficient (d_{33}) of near-stoichiometric lithium niobate after eliminating microdomains increased by 12% compared to congruent lithium niobate. The Curie temperature of near-stoichiometric lithium niobate wafers can reach 1198 °C, and the UV absorption spectrum of near-stoichiometric lithium niobate is blue shifted by 10 nm compared to congruent lithium niobate wafers, making it more suitable for fabricating electro-optic and micro nano electronics devices.

Keywords: X-cut near stoichiometric lithium niobate; diffusion method; refractive index; coercive field

check for updates

Academic Editor: Francisco M. Morales

Received: 20 February 2025
Revised: 8 March 2025
Accepted: 14 March 2025
Published: 19 March 2025

Citation: Dong, Z.; Xu, Q.; Liang, S.; Si, J.; Wang, M.; Zhang, X.; He, J. Research on the Fabrication of X-Cut Near Stoichiometric Lithium Niobate Wafers. *Crystals* **2025**, *15*, 282. https://doi.org/10.3390/cryst15030282

Copyright: © 2025 by the authors. Licensee MDPI, Basel, Switzerland. This article is an open access article distributed under the terms and conditions of the Creative Commons Attribution (CC BY) license (https://creativecommons.org/licenses/by/4.0/).

1. Introduction

The lithium niobate ($LiNbO_3$, LN) crystal is a multifunctional material that embodies electro-optical, piezoelectric, ferroelectric, and pyroelectric properties [1–3]. Currently, LN crystals are extensively utilized in the domains of integrated optics and acoustics [4]. They boast excellent thermal and chemical stability, can be prepared using the Czochralski method, are amenable to processing, and are cost-effective [5]. They stand as one of the few significant functional materials that have sustained relevance over time and continue to pioneer new applications. With a broad, transparent spectral range, a high nonlinear optical coefficient, and a substantial electro-optical coefficient, they have been the subject of extensive research and application in acoustic and optical devices [6,7]. In the field of nonlinear optics, LN crystals can be fashioned into various periodic and quasi-periodic structures and have been widely employed. The output laser wavelength spans from ultraviolet to terahertz frequencies. They are acknowledged as a primary candidate material for "optical silicon" in the optoelectronics era.

LN crystals can be categorized into congruent lithium niobate (CLN) and near-stoichiometric lithium niobate (NSLN). The Li/Nb ratio of a CLN crystal is 48.6/49.4, and its precise chemical formula is ($Li_{0.95}$, $Nb_{0.01}$, $\square_{0.04}$) NbO_3. It exhibits intrinsic defects, including anti-site Nb at a density of $4 \times 10^{19}/cm^3$ and Li vacancies at $16 \times 10^{19}/cm^3$ [8,9]. In contrast, the Li/Nb ratio of NSLN is nearly 1/1, and its molecular formula closely resembles LN. Compared to CLN crystals, NSLN crystals have fewer intrinsic defects, which is evidenced by enhancements such as a 23.2% increase in the nonlinear optical coefficient (d_{33}) [10–12], a 19.3% increase in the electro-optic coefficient ($n_e{}^3 r^{33}$) [10,11], a 21.9% reduction in the optical modulation half-wave voltage (v_π), and a decrease in the coercive field (E_c) from 21 kV/mm to 2 kV/mm [13,14]. Additionally, the inversion domain structure changes from triangular to hexagonal, and the domain walls of the periodic structure are relatively flat. Compared to CLN, NSLN exhibits improved performance across various aspects to some extent.

There are various methods of preparing NSLN, including the lithium-rich melt method, double crucible method, flux method, etc. [15,16]. The double crucible method presents significant challenges due to the vast disparity between crystal and melt components and the complex continuous feeding system, which obstructs crystal growth and restricts commercial production [17]. Similarly, the lithium-rich melt method also suffers from the disparity between crystal and melt components, further complicated by the intricate continuous feeding system, making NSLN crystal growth even more difficult [17,18]. The flux method also faces challenges, with a large difference between crystal and melt components resulting in slow crystal growth, a propensity for defects, and changes in crystal composition as the melt varies [17]. In contrast, the diffusion method is not only able to grow the NSLN crystal relatively simply, but also allows for composition adjustment through solid-phase diffusion on existing crystals, making it compatible for producing large-size and high-quality crystals [17]. However, its drawback lies in the limitation imposed by diffusion speed, leading to prolonged crystal preparation times and challenges in producing thick crystals. Despite these challenges, the diffusion method remains the most commonly used, and the products produced by this method can satisfy the requirements of most industrial applications.

LN wafers for optical applications mainly include Z-cut and X-cut, which can carry a variety of high-performance photonic devices, such as electro-optic modulators, acousto-optic modulators, frequency combs, and classical and quantum nonlinear frequency converters [18–26]. In X-cut or Z-cut LN, efficient frequency conversion can be obtained based on ferroelectric domain engineering [26,27]. Ferroelectric domains typically have parallel and antiparallel structures. Parallel structure refers to the consistent direction of magnetic domains, also known as head-to-head. Anti-parallel structure refers to the inconsistency of magnetic domain directions, also known as tail-to-tail. Antiparallel structures are usually prepared using Z-cut lithium niobate, while parallel and antiparallel structures are usually prepared using X-cut lithium niobate. These latter structures are extensively utilized in domain wall nanoelectronics [27]. Compared to NSLN, the high coercive field of CLN and the uneven domain walls make it challenging to create a periodic structure, resulting in poor quality that hinders its development. Furthermore, compared to Z-cut NSLN, the X-cut NSLN modulator can more effectively leverage the electro-optic coefficient r33 to achieve higher modulation efficiency, enhancing the on-wafer optical systems' capacity. This system is essential for independently modulating light across different wavelength bands [10–12]. Upon completion of growth, CLN crystals manifest a multi-domain state externally, necessitating a single domain process. An external electric field is often applied at high temperatures to accomplish this. NSLN prepared via the diffusion method already possesses single domain characteristics, but a large number of micro-antidomains

persist around defects, such as dislocations, impacting the crystal's electro-optical performance [28]. A secondary external electric field is also required to achieve a single domain state. For Z-cut NSLN, a secondary external electric field is applied to achieve this, and the length of the applied electric field is generally around 1 mm, which is relatively straightforward to implement. However, for X-cut NSLN, due to the high voltage required for the lateral applied electric field, there are only a few reports about this method.

The NSLN fabricated through the diffusion method exhibits macroscopic single-domain characteristics. Employing a quasi-static piezoelectric constant measuring instrument, it has clearly demonstrated macroscopic piezoelectric properties. No research has been performed on the fabrication of X-cut NSLN crystals using the diffusion method so far. We eliminated microdomains inside the wafer by designing an X-cut polarization mold.

2. Experiment

2.1. Diffused Polycrystalline

The diffusion method for preparing NSLN wafers is a process in which Li+ diffuses from Li-rich LN polycrystalline material to CLN wafers at an elevated temperature. The Li content of the diffusion polycrystalline material is a key condition affecting the final NSLN wafer composition. The preparation of LN polycrystalline material involves thoroughly mixing lithium carbonate (Li_2CO_3) and niobium oxide (Nb_2O_5) in a specific molar ratio using a drum ball mill, and then putting it into a high-temperature furnace. The temperature was gradually heated up to 800 °C and maintained for 4 h, followed by a further increase to 1160 °C, where it was held for an additional 4 h to synthesize polycrystalline material. Utilizing this method, the study produced four distinct types of Li-rich LN polycrystalline diffusion materials, with the mixed Li/Nb composition ratios being 58/42, 56/44, 54/46, and 52/48, respectively.

2.2. Preparation of NSLN

The diffused X-cut CLN wafer originates from Ningxia Jujingyuan Crystal Technology Co., Ltd. (Shizuishan, China), featuring specific specifications such as the Curie temperature being 1141.3 °C, a diameter of 100.4 mm, and a thickness of 0.76 mm. The Li/Nb ratio in the LN wafers produced by the company is 48.5/51.5. The preparation process of the NSLN wafer is shown in Figure 1a. The Li-rich LN polycrystalline material is placed on the ceramic lid. The Li-rich atmosphere is supplied to the sealed ceramic crucible via outward diffusion of Li ions at high temperatures. The Li in the air diffused into the CLN wafer and became the NSLN wafer. The sealing space is created by inverting the crucibles inside the crucible and filling the gaps between them with vacuum-sealed powder, which not only serves as a sealant but also prevents the diffusion of Li ions from escaping. The actual picture after installation is shown in Figure 1b.

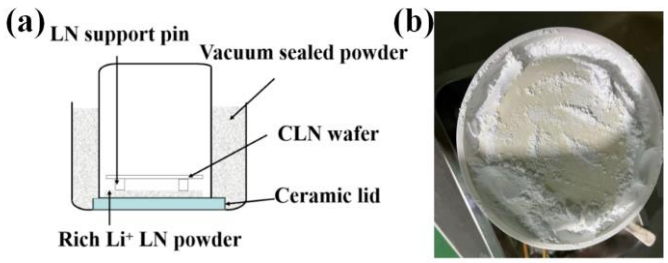


Figure 1. Diffusion diagram. (**a**) Schematic diagram of NSLN wafer preparation; (**b**) Actual picture after assembly.

2.3. Characterization

The wafer's refractive index was assessed using the ES01A apparatus from Beijing Liangtuo Co., Ltd. (Beijing, China), and the sample's refractive index and extinction coefficient across various wavelengths ranging from 300 to 1300 nm were determined. The initial circle, with a diameter of 20 mm, underwent scanning at 4 points, as did the second circle with a diameter of 40 mm. The third circle, with a diameter of 60 mm, and the fourth circle, with a diameter of 80 mm, were also scanned at 4 points each. In total, 17 points, including the central point, were examined, with an incident angle of 70°. The UV-3600 instrument by Shimadzu (Nishinokyo, Tokyo, Japan) was utilized to measure the ultraviolet absorption spectrum of the LN within the 200–800 nm range at an ambient temperature. The crystal diffraction parameters of the LN crystal were evaluated using the D8-Advance X-ray diffractometer (XRD) from Bruker, Germany. The X-ray source used was the Kα ray from a copper target, with an operating voltage and current of 40 kV and 40 mA, respectively, and the scanning angle ranged from 5° to 90°. The same equipment was employed to analyze the diffraction properties of CLN and LN-diffused polycrystalline materials. The d_{33} of CLN and NSLN wafers were tested using the ZJ-3A quasi-static d_{33} tester from the Institute of Acoustics, Chinese Academy of Sciences (Beijing, China).

3. Results and Discussion

3.1. XRD Characterization of Diffusion Materials

Figure 2a depicts the XRD diagram of Li-rich diffusion polycrystalline materials with different Li contents. PDF#75-0907 corresponds to the Li_3NbO_4 phase, while PDF#78-0251 represents the $(Li_{0.941}Nb_{0.059})Nb_{0.9528}O_3$ phase. It is evident that the Li-rich LN polycrystalline diffusion material exhibits an additional distinct diffraction peak at 25.87° when compared to the LN wafer of identical composition. Upon comparison with the PDF standard card, it becomes evident that the supplementary XRD peaks indicate the (211) facet of the Li_3NbO_4 phase [29]. Consequently, the Li-rich LN polycrystalline material comprises both $(Li_{0.941}Nb_{0.059})Nb_{0.9528}O_3$ and Li_3NbO_4 phases. No correlation was found between the half width and peak intensity of the (211) peak and the concentration of Li ions in the powder. We believe that this is caused by the powder being polycrystalline. Figure 2b illustrates the lattice parameters of Li-rich diffusion polycrystalline materials with different Li contents. It is observed that the lattice parameters a and c of the polycrystalline material exhibit a decreasing trend as the Li content increases. In summary, with the rise in Li content of the Li-rich LN polycrystalline material, forming the Li_3NbO_4 phase becomes easier, and this phase formation leads to a reduction in the material's lattice parameters. Lithium niobate crystals belong to the trigonal crystal system, with the *c*-axis being the polar axis of the lithium niobate crystal. The diffusion of Li ions reduces many Li vacancy defects and Nb anti-site defects. Both of these defects have a significant impact on lattice parameter a and a minor impact on lattice parameter *c* [30–33].

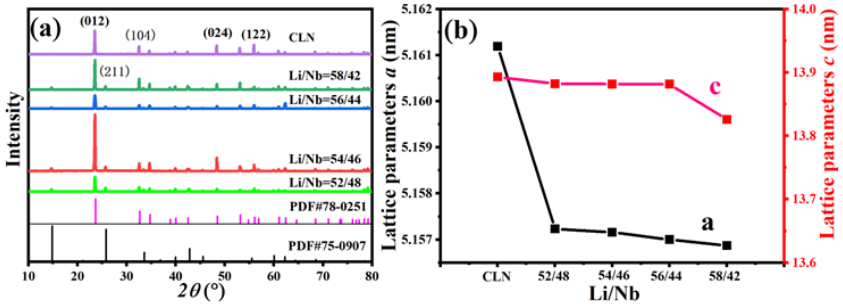


Figure 2. (**a**) XRD patterns of Li-rich diffused polycrystalline materials with different Li content; (**b**) lattice parameters of Li-rich diffused polycrystalline materials with different Li content.

3.2. Discussion on Wafer Diffusion Process

The diffused wafers are X-cut CLN wafers produced in the same batch. The main change in the diffusion process is the diffusion temperature, which is 1210 °C, 1195 °C, 1180 °C, and 1160 °C, respectively. The heating rate is 50 °C/min, and the diffusion time is 60 h. The Li/Nb ratio in Li-rich LN polycrystalline material used is 58/42, 56/44, and 54/46, and the mass of the diffused polycrystalline material equaled 100 g for all samples. Table 1 illustrates the diffusion process of the NSLN wafer.

Table 1. Diffusion process and results of NSLN wafers.

Diffusion Powder	Holding Temperature	State of the Wafer to Be Diffused	As Shown in the Figure 3
Li/Nb = 58/42	1210 °C	Almost all melted	Figure 3a
Li/Nb = 58/42	1195 °C	Mostly melted	Figure 3b
Li/Nb = 56/44	1195 °C	A small part is melted, the wafer is incomplete, $d_{33} = 10.5 \times 10^{-12}$ C/N	Figure 3c
Li/Nb = 54/46	1180 °C	not melted, Complete, $d_{33} = 10.8 \times 10^{-12}$ C/N	Figure 3d
Li/Nb = 56/44	1160 °C	Complete, $d_{33} = 0$	Figure 3e

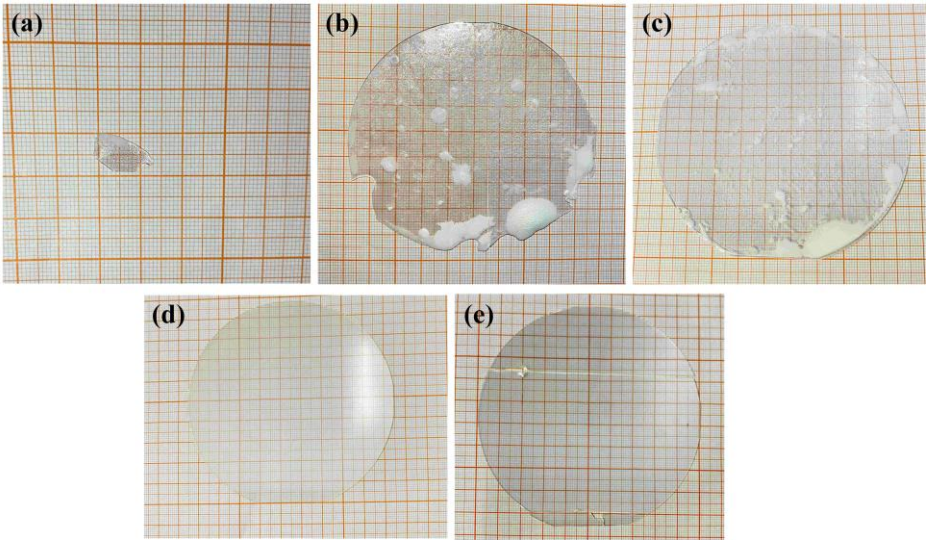


Figure 3. The actual diagram of NSLN wafer obtained by different diffusion conditions. (**a**) Li/Nb = 58/42, the diffusion temperature was 1210 °C; (**b**) Li/Nb = 58/42, the diffusion temperature was 1195 °C; (**c**) Li/Nb = 56/44, the diffusion temperature was 1195 °C; (**d**) Li/Nb = 54/46, the diffusion temperature was 1180 °C; (**e**) Li/Nb = 56/44, the diffusion temperature was 1160 °C.

Figure 3 shows the state of the wafers following the diffusion process. It is evident that the wafer has been through a significant melting process at a diffusion temperature of 1210 °C.

At 1195 °C, the edge of the wafer exhibits melting, and white protrusions are present on its surface. It is worth noting that the higher the Li content in the diffusion material, the more pronounced the white protrusions will become. At 1180 °C, the wafer's surface remains unmelted and free of any foreign substances. Similarly, at 1160 °C, the surface of the wafer did not melt and there were no foreign objects, but $d_{33} = 0$ was measured, which means that the wafer did not reach the stoichiometric ratio.

The experimental results indicate that the melting point of an LN wafer is 1210 °C. However, due to the diffusion of Li ions into the wafer, the melting point of the wafer's

surface is diminished. At 1210 °C, the wafer is nearly entirely melted. Concurrently, the volatilization rate of Li further reduces the melting point of the wafer's surface. At a temperature of 1195 °C, with a Li/Nb ratio of 58/42, the wafer's surface also undergoes the melting process. Likewise, diffusion materials with Li/Nb ratios of 58/42 and 56/44 were utilized. It was observed that when a diffusion material with Li-rich content is employed at elevated temperatures, white protrusions emerge on the wafer's surface. This is an indication that the wafer will rapidly melt once it becomes Li-rich [34]. Subsequently, diffusion was conducted at 1160 °C. The Li diffusion rate is slower, and the piezoelectric effect is not externally manifested under the same condition. We implemented pre-diffusion at 1160 °C, followed by a gradual increase in the diffusion temperature to 1180 °C. The wafer remained unmelted, and the NSLN exhibited characteristics of a single domain, which is considered to be a favorable outcome.

3.3. Micro Domain Elimination Process and Single Domain Characterization

The coercive field of a Z-cut NSLN wafer at room temperature ranges from 3000 to 4000 V/mm [35]. The diffusion in this experiment is an X-cut NSLN wafer with a diameter of 100 mm, and microdomain polarization requires an electric field component along the Z direction.

To polarize X-cut NSLN wafers, we designed a specialized fixture 4 for X-cut NSLN. The structure is shown in Figure 4. The Figure 4 components include insulating plastic coated with metal electrodes, insulating rubber rings, and conductive LiF solution. The LiF solution is separated from the wafer by the sealing of the rubber rings. An electric field is added to the metal electrodes, which has a component in the Z direction of the wafer and polarizes the microdomains inside the wafer through this electric field component.

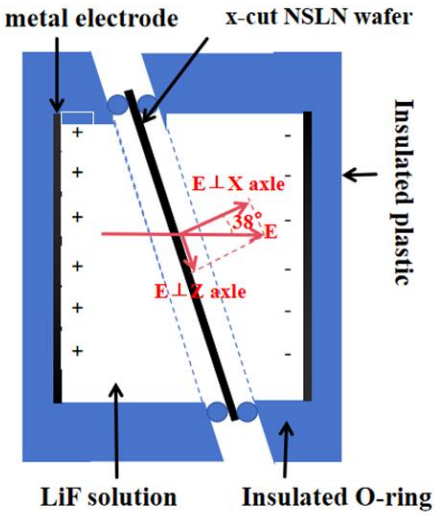


Figure 4. Schematic diagram of liquid polarization.

To prove that the microdomains inside the wafer have reversed, the hysteresis loop of the wafer was tested. Due to the difficulty in testing the coercive field of the X-cut NSLN wafer, a fixture with a 38° angle was designed to test the hysteresis loop of the wafer. Its hysteresis loop is shown in Figure 5. As shown in Figure 5, its coercive field (E_c) is 4423 V/mm, and its Z-direction component is:

$$E_c(\mathrm{Z}) = E_c \times \sin 38^\circ \quad (1)$$

Therefore, its coercive field is 2723 V/mm. Compared with the coercive field of CLN wafers, it has a significant reduction, which proves that its microdomains have been eliminated.

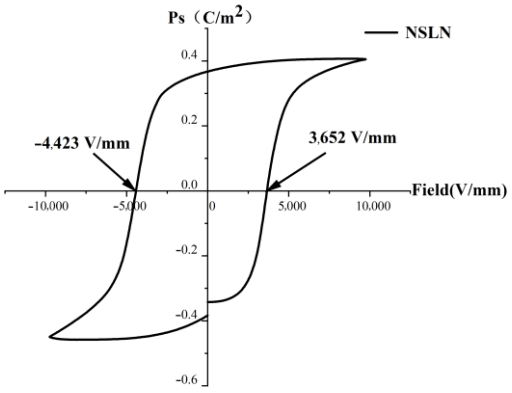


Figure 5. NSLN wafer coercive field.

Upon immersing the single-domain wafer in a dilute nitric acid solution, the silver-coated electrode is extracted, carefully cleaned, and subsequently dried. The measurement of the value is then conducted along the Z-axis using a quasi-static d_{33} detector (model ZJ-3A) supplied by the Institute of Acoustics at the Chinese Academy of Sciences (Beijing, China). For comparative purposes, we employ CLN and non-secondary polarized samples. The results of these tests are presented in Table 2.

Table 2. Piezoelectric coefficients of samples in different states.

Sample	$d_{33}/(\times 10^{-12}$ C/N)
CLN	9.7
Non-polarized NSLN	10.4
Polarized NSLN	10.8

As evidenced by Table 2, the piezoelectric parameter for CLN is 9.7 $\times$ 10^{-12} C/N, while that of unpolarized NSLN stands at 10.4 $\times$ 10^{-12} C/N, and polarized NSLN exhibits a parameter of 10.8 $\times$ 10^{-12} C/N. In essence, the piezoelectric parameters of NSLN post-diffusion experience a significant enhancement, with an additional increase observed following the polarization process.

3.4. Curie Temperature Test

Curie temperature is a crucial physical parameter for ferroelectric materials, signifying the transition from a ferroelectric state to a paraelectric state as the material is heated [35–38]. The Curie point of LN crystals corresponds to the temperature at which the phase transition occurs. Typically, this temperature is influenced by the Li/Nb ratio within the crystal, making it an essential measure of the internal composition of LN. Given that the characteristics of ferroelectric crystals undergo alterations above and below the Curie temperature, the Curie temperature of LN crystals can be determined through a variety of methods. One such method involves monitoring changes in the dielectric constant. The dielectric constant is notably high near the crystal's Curie point, allowing the determination of the sample's Curie temperature by identifying the anomalous values at this juncture. Utilizing a high-temperature dielectric measurement instrument, the Curie temperature of an X-cut NSLN wafer was tested at frequencies of 100 kHz, 500 kHz, and 1000 kHz, respectively (as shown in Figure 6). Under these varying frequency conditions, the Curie temperature measured by the NSLN wafer was found to be 1198 °C, which indicates a

significant increase in the internal Li content of the NSLN wafer fabricated via the diffusion method, close to the stoichiometric ratio determined by chemical analysis. The relationship between Li ion concentration inside the chip and Curie temperature has been summarized by Masaru Nakamura [39]. The relationship is shown in Formula (2):

$$C_{Li} = 24.598 + 0.020925T_c \quad (2)$$

As the concentration of Li ions inside the chip increases, the Curie temperature also rises. Compared with the literature of Masaru Nakamura, the Li/(Li + Nb) ratio in the NSLN prepared is 49.6% [39].

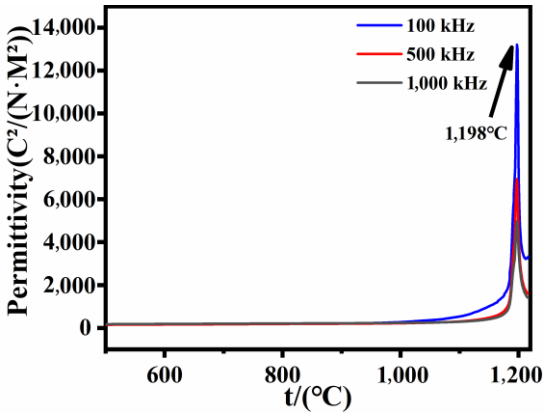


Figure 6. Curie temperature measured by NSLN at different frequencies.

3.5. UV Absorption Spectrum

An electromagnetic wave with a specific wavelength within the ultraviolet-visible (UV-Vis) spectrum corresponds to a particular level of radiation energy. Both ultraviolet and visible light are capable of exciting valence electrons, notably π electrons, boosting their transition to higher energy states. Consequently, the UV-Vis spectrum primarily reflects alterations in the energy levels of electrons within molecules. The composition of crystals can be determined through analysis of their ultraviolet absorption spectra [39,40]. As shown in Figure 7, in comparison to CLN, the ultraviolet absorption edge of the NSLN wafer moves about 11 nm toward the ultraviolet region compared to the CLN wafer.

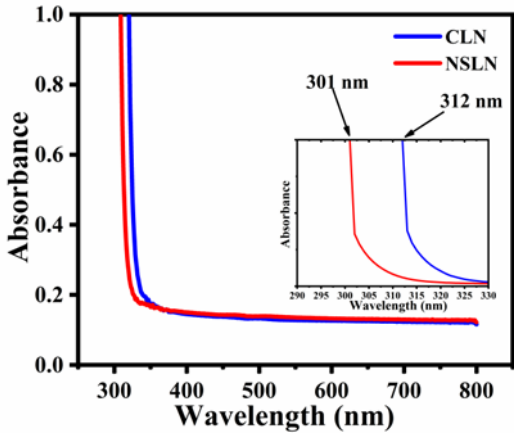


Figure 7. UV-Vis absorption spectra of CLN and NSLN wafer.

LN crystals, which are oxygen-containing octahedral ferroelectrics, have their fundamental optical absorption edge primarily determined by the transition energy between the valence band and the conduction band. In this context, the valence band corresponds to

the 2p orbital of oxygen, while the conduction band is represented by the empty d orbital of Nb^{5+}. Consequently, alterations in the electron cloud distribution of the coordinated oxygen atoms can influence the position of the absorption edge [41]. Within LN crystals, two primary types of defects are prevalent: Li vacancies and Nb antisite defects. As the Li/Nb ratio within the crystal rises, the prevalence of Nb antisite defects diminishes. Since the polarization capacity of Li ions is significantly lower than that of Nb^{5+} ions, the energy required for electron transitions from the 2p orbital of O^{2-} to the vacant d orbital of Nb^{5+} increases, leading to a blue shift in the absorption edge, which means that the NSLN wafer possesses greater potential in the application of ultraviolet spectroscopy than the CLN wafer does [35].

3.6. Refractive Index

The refractive index of the wafer was measured using the ES01A ellipsometer. The sampling points are shown in Figure 8, and the refractive index was measured at a distance of 10 mm between two adjacent test points, as shown in Table 3. It can be seen that the average refractive index of the NSLN wafer under 632.8 nm light is 2.2996. The refractive index gradient of the NSLN wafers can be determined by using the refractive index data of the NSLN wafers. As evident from Table 3, the NSLN wafer exhibits smaller transverse and longitudinal refractive index gradients, indicating superior optical uniformity. This characteristic confers significant application benefits for the fabrication of electro-optical devices.

Table 3. Measurement results of NSLN refractive index.

Serial Number	Refractive Index n of NSLN (@632.8 nm)
1	2.3044
2	2.2932
3	2.2992
4	2.3015
5	2.3035
6	2.2992
7	2.2920
8	2.2972
9	2.3006
10	2.2992
11	2.2845
12	2.3047
13	2.3001
14	2.3049
15	2.3044
16	2.3035
17	2.3017
Average value	2.2996
Transverse mean$\Delta n_{16\text{-}14}$	1.75×10^{-4}/cm
Longitudinal mean$\Delta n_{17\text{-}15}$	3.375×10^{-4}/cm

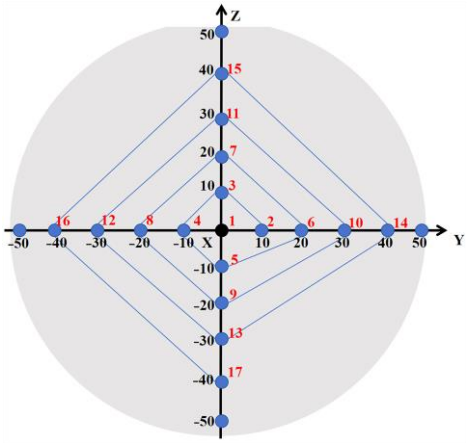


Figure 8. Sampling diagram used to test the refractive index of the sample.

4. Summary

This article used the diffusion method to fabricate the NSLN wafers, ensuring that the surface of the NSLN wafers was free from twins and cracks by controlling process parameters. It was observed that at a diffusion temperature of 1180 °C, the prepared surface exhibited no twins and possessed piezoelectric properties, resulting in a NSLN wafer with these characteristics. The Li-rich polycrystalline material consisted of $(Li_{0.941}Nb_{0.059})Nb_{0.9528}O_3$ and Li_3NbO_4. As the Li content increased, the lattice parameters a and c of the Li-rich polycrystalline material decreased. The NSLN wafer produced had a higher internal Li content, close to the stoichiometric ratio of Li, and the Curie temperature of the NSLN was 1198 °C. The coercive field of NSLN wafers was less than that of CLN wafers. The UV absorption spectrum of NSLN was blue-shifted by 10 nm compared to CLN. The refractive index of NSLN was higher than that of CLN, and the refractive index gradient was smaller than that of CLN, resulting in better optical uniformity on the NSLN lenses, which means that NSLN wafers possess greater potential in the application of ultraviolet spectroscopy than CLN wafers do.

Author Contributions: Conceptualization, M.W., Z.D. and Q.X.; methodology, M.W. and J.S.; validation, S.L.; formal analysis, J.H. and X.Z.; writing—review and editing, J.S. and Q.X.; funding acquisition, J.H. and X.Z. All authors have read and agreed to the published version of the manuscript.

Funding: This work was sponsored by Zhongyuan Critical Metals Laboratory (grant number ZYGJJS2023002).

Data Availability Statement: The raw data supporting the conclusions of this article will be made available by the authors on request.

Acknowledgments: The authors thank Zhongyuan Critical Metals Laboratory (grant number ZYGJJS2023002).

Conflicts of Interest: Authors Shuaijie Liang and Jiashun Si were employed by the company Ningxia Ju Jing Yuan Crystal Technology Company. The remaining authors declare that the research was conducted in the absence of any commercial or financial relationships that could be construed as a potential conflict of interest.

References

1. Lyu, J.B.; Zhu, T.; Zhou, Y.; Chen, Z.M.; Pi, Y.Z.; Liu, Z.T.; Xu, X.C.; Xu, K.; Ma, X.; Wang, L.; et al. Inverse design for material anisotropy and its application for a compact X-cut TFLN on-chip wavelength demultiplexer. *OES* **2023**, *2*, 230038–230041. [CrossRef]
2. Cheng, W.; Mian, Z.; Xi, C.; Bertrand, M.; Shams-Ansari, A.; Chandrasekhar, S.; Winzer, P.; Loncar, M. Integrated lithium niobate electro-optic modulators operating at CMOS-compatible voltages. *Nature* **2018**, *562*, 101–104. [CrossRef]

3. Zhu, D.; Shao, L.B.; Yu, M.J.; Cheng, R.; Desiaov, C.J.; Xu, Y.W.; Holzgrafe, J.; Ghosh, S.; Shams-Ansari, A.; Puma, E.; et al. Integrated photonics on thin-film lithium niobate. *Adv. Opt. Photonics* **2021**, *13*, 242–352. [CrossRef]
4. Lengyel, K.; Péter, Á.; Kovács, L.; Corradi, G.; Pálfalvi, L.; Hebling, J.; Unferdorben, M.; Dravecz, G.; Hajdara, I.; Szaller, Z.; et al. Growth, defect structure, and THz application of stoichiometric lithium niobate. *Appl. Phys. Rev.* **2015**, *2*, 040601. [CrossRef]
5. Mercante, A.J.; Shi, S.; Yao, P.; Xie, L.L.; Weikle, R.; Prather, D. Thin film lithium niobate electro-optic modulator with terahertz operating bandwidth. *Opt. Express* **2018**, *26*, 14810. [CrossRef]
6. Rao, A.; Patil, A.; Rabiei, P.; Honardoost, A.; DeSalvo, R.; Paolella, A.; Fathpour, S. High-performance and linear thin-film lithium niobate Mach–Zehnder modulators on silicon up to 50 GHz. *Opt. Lett.* **2016**, *41*, 5700–5703. [CrossRef]
7. Toro, J.A.; Serrano, M.D.; Cabañes, A.G.; Cabrera, J.M. Accurate interferometric measurement of electro-optic coefficients: Application to quasi-stoichiometric $LiNbO_3$. *Opt. Commun.* **1998**, *154*, 23–27. [CrossRef]
8. Iyi, N.; Kitamura, K.; Izumi, F.; Yamamoto, J.K.; Hayashi, T.; Asano, H.; Kimura, S. Comparative study of defect structures in lithium niobate with different compositions. *J. Solid State Chem.* **1992**, *101*, 340–352. [CrossRef]
9. Kong, Y.; Bo, F.; Wang, W.; Zheng, D.; Liu, H.; Zhang, G.; Rupp, R.; Xu, J. Recent progress in lithium niobate: Optical damage, defect simulation, and on-chip devices. *Adv. Materi.* **2020**, *32*, 1806452. [CrossRef]
10. Fujiwara, T.; Takahashi, M.; Ohama, M.; Ikushima, A.J.; Furukawa, Y.; Kitamura, K. Comparison of electro-optic effect between stoichiometric and congruent $LiNbO_3$. *Electro. Lett.* **1999**, *35*, 499–501. [CrossRef]
11. Xue, D.; Zhang, S. The effect of stoichiometry on nonlinear optical properties of $LiNbO_3$. *J. Phys. Condens. Matter* **1997**, *9*, 7515. [CrossRef]
12. Klein, R.S.; Kugel, G.E.; Maillard, A.; Plgar, K.; Peter, A. Absolute non-linear optical coefficients of $LiNbO_3$ for near stoichiometric crystal compositions. *Opt. Mater.* **2003**, *22*, 171–174. [CrossRef]
13. Xiong, X.; Cao, Q.-T.; Xiao, Y.-F. Thin-film lithium niobate photonic integrated devices: Advances and oppotunities. *Acta Phys. Sin.* **2023**, *72*, 234201. [CrossRef]
14. Ganesamoorthy, S.; Nakamura, M.; Takekawa, S.; Kumaragurubaran, S.; Terabe, K.; Kitamura, K. A comparative study on the domain switching characteristics of near stoichiometric lithium niobate and lithium tantalate single crystals. *Mater. Sci. Eng. B* **2005**, *120*, 125–129. [CrossRef]
15. Sidorov, N.V.; Antonycheva, E.A.; Syuĭ, A.V.; Palatnikov, M.N. Photorefractive properties of stoichiometric lithium niobate single crystals. *Crystallogr. Rep.* **2010**, *55*, 1019–1024. [CrossRef]
16. Xiao, X.; Si, J.; Liang, S.; Xu, Q.; Zhang, H.; Ma, L.; Yang, C.; Zhang, X. Preparation, Properties, and Applications of Near Stoichiometric Lithium Tantalate Crystals. *Crystals* **2023**, *13*, 1031. [CrossRef]
17. Furukawa, Y.; Kitamura, K.; Ji, Y.; Zgonik, M.; Medrano, C.; Günter, P. Photorefractive properties of iron-doped stoichiometric lithium niobate. *Opt. Lett.* **1997**, *22*, 501–503. [CrossRef]
18. Elkus, B.S.; Abdelsalam, K.; Rao, A.; Velev, V.; Fathpour, S.; Kumar, P.; Kanter, S. Generation of broadband correlated photon-pairs in short thin-film lithium-niobate waveguides. *Opt. Express* **2019**, *27*, 38521–38531. [CrossRef]
19. Zhao, J.; Ma, C.; Rüsing, M.; Mookherjea, S. High Quality Entangled Photon Pair Generation in Periodically Poled Thin-Film Lithium Niobate Waveguides. *Phys. Rev. Lett.* **2020**, *124*, 163603. [CrossRef]
20. Chen, J.; Meng Sua, Y.; Ma, Z.; Tang, C.; Zhan, L.; Yu, P.H. Efficient parametric frequency conversion in lithium niobate nanophotonic chips. *OSA Contin.* **2019**, *2*, 2914. [CrossRef]
21. Lu, J.; Surya, J.; Liu, X.; Bruch, A.; Gong, Z.; Xu, Y.; Tang, H. Periodically poled thin-film lithium niobate microring resonators with a secondharmonic generation efficiency of 250,000%/W. *Optica* **2019**, *6*, 1455. [CrossRef]
22. Chen, J.; Ma, Z.; Sua, Y.; Li, Z. Ultra-efficient frequency conversion in quasi-phase-matched lithium niobate microrings. *Optica* **2019**, *6*, 1244. [CrossRef]
23. Wang, C.; Langrock, C.; Marandi, A.; Jankowski, M. Ultrahigh-efficiency wavelength conversion in nanophotonic periodically poled lithium niobate waveguides. *Optica* **2018**, *5*, 1438. [CrossRef]
24. Zhang, M.; Buscaino, B.; Wang, C.; Shams-Ansari, A.; Reimer, C.; Zhu, R.; Kahn, J.; Lončar, M. Broadband electro-optic frequency comb generation in a lithium niobate microring resonator. *Nature* **2019**, *568*, 373–377. [CrossRef]
25. Wang, C.; Zhang, M.; Yu, M.; Zhu, R.; Hu, H.; Loncar, M. Monolithic lithium niobate photonic circuits for Kerr frequency comb generation and modulation. *Nat. Commun.* **2019**, *10*, 978. [CrossRef]
26. Lu, Y.; Wei, T.; Duewer, F.; Lu, Y.; Ming, N.; Schultz, P.; Xiang, X. Nondestructive imaging of dielectric-constant profiles and ferroelectric domains with a scanning-tip microwave near-field microscope. *Science* **1997**, *276*, 2004–2006. [CrossRef]
27. Liu, Q.; Song, Y.; Bai, L.; Zhang, L.; Chen, X.; Zhao, X.; Wang, F.; Liu, H.; Wang, D.; Li, Y.; et al. Promoting Periodical Poling in Lithium Niobate Crystal Through Surface Acoustic Wave-Induced Local Lattice Activation. *Laser Photonics Rev.* **2024**, *18*, 2400248. [CrossRef]
28. Wada, S.; Kakemoto, H.; Tsurumi, T. Enhanced piezoelectric properties of piezoelectric single crystals by domain engineering. *Mater. Trans.* **2004**, *45*, 178–187. [CrossRef]

29. Wang, D.; Hao, Z.; Zhu, X.; Zhou, F.; Shu, Y.; He, J. Spheroidization of lithium niobate powder by radio-frequency inductively coupled plasma. *Ceram. Int.* **2022**, *48*, 12126–12131. [CrossRef]
30. Schirmer, O.F.; Imlau, M.; Merschjann, C.; Schoke, B. Electron small polarons and bipolarons in $LiNbO_3$. *J. Condens. Matter Phys.* **2009**, *21*, 123201. [CrossRef]
31. Nahm, H.H.; Park, C.H. First-principles study of microscopic properties of the Nb antisite in $LiNbO_3$: Comparison to phenomenological polaron theory. *Phys. Rev. B* **2008**, *78*, 184108. [CrossRef]
32. Maaider, K.; Masaif, N.; Khalil, A. Stoichiometry-related defect structure in lithium niobate and lithium tantalate. *Indian J. Phys.* **2020**, *95*, 275–280. [CrossRef]
33. Masaif, N.; Jebbari, S.; Bennani, F. Experimental and analytical study of defect structures in nonstoichiometric lithium tantalate and lithium niobate. *Phys. Status Solidi (B)* **2003**, *3*, 640–648. [CrossRef]
34. Yang, J.F.; Zhang, H.; Xu, H.X.; Huang, S.L.; Zhang, L.; Sun, J.; Huang, C.X.; Kong, Y.F.; Xu, J.J. Study on the diffusion of reverse niobium in lithium niobate crystals with the same composition. *J. Synth. Cryst.* **2015**, *44*, 3379–3383. [CrossRef]
35. Kim, S.; Gopalan, V.; Gruverman, A. Coercive fields in ferroelectrics: A case study in lithium niobate and lithium tantalate. *Appl. Phys. Lett.* **2002**, *80*, 2740–2742. [CrossRef]
36. Shen, Z.; Li, J. Enhancement of piezoelectric constant d_{33} in $BaTiO_3$ ceramics due to nano-domain structure. *J. Ceram. Soc. Jpn.* **2010**, *118*, 940–943. [CrossRef]
37. Dong, Y.; Zhou, Z.; Liang, R.; Dong, X. Excellent piezoelectric constant and thermal stability in $BiScO_3$–$PbTiO_3$ piezoelectric ceramics via domain engineering. *J. Mater.* **2022**, *8*, 319–326. [CrossRef]
38. Xiao, X.; Xu, Q.; Liang, S.; Zhang, H.; Ma, L.; Hai, L.; Zhang, X. Preparation and defect structure analysis of near-stoichiometric lithium tantalate wafers. *RSC Adv.* **2022**, *12*, 19091–19100. [CrossRef]
39. Nakamura, M.; Takekawa, S.; Kumaragurubaran, S.; Kitamura, K. Curie temperature and [Li]/([Li]+[Nb]) ratio of near-stoichiometric $LiNbO_3$ crystal grown from different Li-rich solutions. *Jpn. J. Appl. Phys* **2008**, *47*, 3476. [CrossRef]
40. Kovács, L.; Ruschhaupt, G.; Polgár, K.; Corradi, G.; Wöhlecke, M. Composition dependence of the ultraviolet absorption edge in lithium niobate. *Appl. Phys. Lett.* **1997**, *70*, 2801–2803. [CrossRef]
41. Bäumer, C.; David, C.; Tunyagi, A.; Betzler, K.; Hesse, H.; Krätzig, E.; Wöhlecke, M. Composition dependence of the ultraviolet absorption edge in lithium tantalate. *J. Appl. Phys.* **2003**, *93*, 3102–3104. [CrossRef]

Disclaimer/Publisher's Note: The statements, opinions and data contained in all publications are solely those of the individual author(s) and contributor(s) and not of MDPI and/or the editor(s). MDPI and/or the editor(s) disclaim responsibility for any injury to people or property resulting from any ideas, methods, instructions or products referred to in the content.